Modeling of time-resolved LIBS spectra obtained in Martian atmospheric conditions with a stationary plasma approach

P.B. Hansen [a,*], S. Schröder [a,*], S. Kubitza [a], K. Rammelkamp [a,b], D.S. Vogt [a], H.-W. Hübers [a,c]

[a] *Deutsches Zentrum für Luft- und Raumfahrt e.V. (DLR), Institut für Optische Sensorsysteme, Rutherfordstraße 2, 12489 Berlin, Germany*
[b] *Institut de Recherche en Astrophysique et Planétologie, 9 avenue du Colonel Roche, 31028 Toulouse, France*
[c] *Humboldt-Universität zu Berlin, Institut für Physik, Newtonstraße 15, 12489 Berlin, Germany*

ABSTRACT

In this study, we investigate the characteristics of the LIBS plasma in Martian atmospheric conditions using stationary modeling of the LIBS plasma. LIBS spectra are simulated from a one-dimensional model of the plasma divided into two zones along the line of sight. The simulations are based on local thermal equilibrium and carried out using radiative transfer. The simulated spectra are fitted first to synthetic LIBS spectra to test the implementation and in a second step to time-resolved LIBS data of a carbonate sample obtained in experimentally simulated Martian atmospheric conditions. From the fits to the synthetic LIBS spectra, we confirm that plasmas with spatial gradients in the temperature and densities can be well described in a two-zone plasma model. From the fits to the measured data this observation also holds true. We find that the most of the emission lines are well described in the two-zone model and that the two-zone model is a significant improvement from the one-zone model. Furthermore, we obtain typical values of the plasma properties in the two-zone approximation from 500 ns to 1250 ns after plasma initiation and derive the effect of self-absorption, which is predicted to decrease the strongest pixel intensities by a factor of almost two orders of magnitudes.

1. Introduction

Laser induced breakdown spectroscopy (LIBS) has been proven very useful for in-situ geochemical analysis on the Martian surface with the ChemCam instrument onboard the Curiosity rover [1]. Two more rover-based missions to Mars were launched in summer 2020. Both rovers carry LIBS instruments as part of their instrument payloads [2,3], showing the interest of the planetary community in this technique and the benefits of an improved understanding of the Martian LIBS data.

In general, the characteristics of the LIBS plasma, such as its lifetime, temperature, species distributions and densities, provide useful information for analyzing the LIBS data and building calibration models. Such characteristics strongly depend on the ambient atmospheric conditions [4]. Many insights obtained from characterizing the LIBS plasma in argon or Earth's atmosphere are therefore not directly applicable to the LIBS data acquired in the Martian atmosphere. In order to improve the analysis of Martian LIBS spectra, specific studies in Martian atmospheric conditions are necessary.

Most approaches for characterizing the LIBS plasma are based on the assumption of local thermodynamic equilibrium (LTE) [5]. In LTE, the degree of ionization and the atomic state distributions are described completely by the plasma properties: the plasma temperature and species densities. The validity of the assumption of LTE in the highly transient LIBS plasma is discussed widely in the literature with the general conclusion that LTE can only be considered as a good approximation under certain experimental conditions at specific time intervals after plasma initiation [5,6]. Nonetheless, due to the simplicity of the description of the plasma in LTE, it is usually favored over the alternative, a complete kinetic description of the population and depopulation of the states via the processes of photo-ionization; radiative and three-body recombination; collisional excitation/de-excitation processes; radiative decay; photo-excitation and bremsstrahlung [5].

The most common LTE approaches to obtain the plasma temperature are the methods of Boltzmann or Saha-Boltzmann plots. Both methods are based on the relative intensities of emission lines originating from different upper electronic levels [7]. Other approaches are based on computational simulations of the LIBS plasma dynamics [8,9]. The simulations are usually split into two parts where the first part describes the process of laser ablation and the second part describes the following expansion of the plasma into the ambient gas using hydrodynamic

modeling. Such simulations provide insight into the plasma dynamics, such as the formation of shock waves; partitioning of energy; temperature and density distributions inside the plasma. A third method consists of fitting spectra, simulated from a model of the plasma, to measured data, i.e. solving the inverse problem. In such case a stationary model of the plasma based on LTE is more practical than the dynamic models due the much lower complexity of the stationary model where the temporal description is omitted. Hermann et al. [10] simulated spectra from a stationary two-zone LTE plasma model and fitted them to time resolved spectra of an aluminium and a titanium-sapphire sample. Spectra were acquired in both Earth's atmosphere and in an argon gas at a pressure of $5 \cdot 10^4$ Pa. The two-zone plasma model consists of two homogeneous zones intended to describe the plasma core and periphery. Hermann et al. found that the two-zone LTE model described the data well and that the plasma induced in the argon gas was almost homogeneous. In contrast, temperature and density gradients were evident in air, which is in agreement with both dynamic modelings and results from spatially resolved temperature estimates using the method of Boltzmann plots [9,11].

In this study, a similar approach as the one of Hermann et al. is used to investigate the characteristics of the LIBS plasma in Martian atmospheric conditions. LIBS spectra are simulated from a stationary two-zone LTE plasma model and fitted to both synthetic and measured time resolved LIBS spectra of a carbonate sample acquired in experimentally simulated Martian atmospheric conditions. The method of simulating and fitting spectra is applied to synthetic spectra in order to test the implementation and to assess how continuously varying plasma properties are approximated in a two-zone plasma model. The method is then applied to the measured LIBS data where we obtain typical values of the plasma properties, temperature and electron density, for different times after plasma initiation. From the plasma properties, we derive the effect of self-absorption in the spectra. Together with the plasma properties, concentration estimates are obtained as outputs from the fits. We compare the estimated concentrations to the reference values and finally discuss the usefulness of LTE plasma models for the analysis of real mission data. Section 2 describes the plasma model and Section 3 the fitting procedure. In Section 3 and 4 are the results from fits to the synthetic and measured LIBS data presented. The last section contains the conclusion.

2. Plasma modeling and simulation of LIBS spectra

2.1. Plasma modeling

The model, which is used to simulate the spectra, is based on a stationary plasma in local thermal equilibrium (LTE) and the plasma is assumed non-reactive, therefore neglecting the formation of molecules. In LTE, the state of the plasma is described by a set of plasma properties, the plasma temperature and electron density, through the standard equilibrium distributions [5]. The modeling of the plasma is thereby reduced to modeling the plasma properties and elemental densities inside the plasma.

The LIBS set-up used in this study (described in Section 5.1) captures the plasma emission from the direction parallel to the surface normal of the sample and with a narrow field of view and a small acceptance angle. This light collection geometry will be approximated by a single line of sight (LOS) through the plasma-center and the plasma is therefore only modeled in one dimension along this LOS. Along the LOS, the plasma is assumed to be composed of a series of homogeneous zones. While plasma temperature, electron density and lengths of the zones can vary independently from zone to zone, the elemental densities are constrained to follow the same distribution resulting in equal relative elemental concentrations in all the zones;

$$\frac{n_{i,zone_1}}{n_{j,zone_1}} = \frac{n_{i,zone_2}}{n_{j,zone_2}} = \dots \ , \tag{2.1}$$

where i and j refer to the elements. A schematic drawing of such a plasma is shown in Fig. 1. The elemental densities are modeled by the elemental densities in the first zone, $n_{s,0}$, which is closest to the sample surface, and are given as relative values by the relative distribution n_{rel} in the following zones. n_{rel} is thereby equal for all elements but can vary independently from zone to zone. As example, the concentration of element i in zone k is given as:

$$n_{i,zone_k} = n_{i,0} \cdot n_{rel,k} \ . \tag{2.2}$$

With this model of the plasma, spectra are simulated and the model parameters are fitted to synthetic test spectra and to measured time-resolved LIBS. Fits are done using one or two zones, while synthetic test spectra are generated using a large number of zones in order to simulate a continuous plasma ensuring that the robustness of the simplified two-zone model can be easily evaluated. The elements in the plasma that are also originating from the atmosphere (mainly CO_2) are likely to be over represented in the outer region of the plasma and will therefore not follow the same distribution as the elements of the target material (eq. 2.1). Consequently, emission lines from the atmospheric elements (C,O) are not considered in any of the performed fits and only relative concentrations can be derived for samples containing C or O. In such cases, the concentrations of the remaining elements are rescaled to add up to 100%.

2.2. Simulation of LIBS spectra

The simulations of the LIBS spectra are based on the radiance calculated from the one dimensional radiative transfer along the LOS of the plasma model. For the radiative transfer only the processes of spontaneous emission, stimulated emission, and absorption are considered and the radiance from other processes such as recombination and bremsstrahlung are neglected. A description of the calculation of atomic state populations, necessary for evaluating the rates of the considered radiative processes, and a description of the calculation of the LOS radiance, are given in the supplementary material.

In order to make the simulated and measured data comparable, the measured LIBS spectra are corrected by the instrument response of the LIBS set-up. The instrument response is a function of wavelength and covers the transformation from counts in the detector to photons emitted by a source. As the instrument response was determined relatively at different wavelengths, and not absolutely, there will be a constant factor
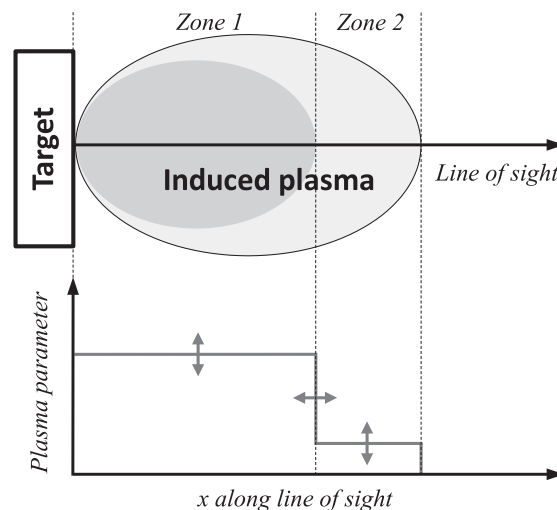

Fig. 1. Schematic drawing of the LIBS plasma divided into two homogeneous zones along the line of sight through the center of the plasma (top). Additionally, it is shown how the plasma properties may vary from zone to zone (bottom).

between a simulated and a calibrated measured spectrum. The cross section of the LOS and exposure time of the measurement are fused into this factor, which will be referred to as the instrumental factor F. Furthermore, the set-up leads to spectral broadening, which will be approximated by the convolution of a Gaussian function.

A simulated spectrum is written as

$$\widetilde{I}_\lambda\left(F, \overrightarrow{T}, \overrightarrow{n}_e, \overrightarrow{n}_0, \overrightarrow{n}_{rel}, \overrightarrow{\Delta x}\right) = F \cdot I_\lambda\left(\overrightarrow{T}, \overrightarrow{n}_e, \overrightarrow{n}_0, \overrightarrow{n}_{rel}, \overrightarrow{\Delta x}\right) * b_\lambda \ , \qquad (2.3)$$

I_λ is the LOS radiance calculated by radiative transfer (see the supplementary material), $\overrightarrow{T}$ is a vector that contains the temperatures of the zones, $\overrightarrow{n}_e$ the electron densities of the zones, $\overrightarrow{n}_0$ the elemental densities in the first zone, $\overrightarrow{n}_{rel}$ the relative elemental concentration in the following zones, $\overrightarrow{\Delta x}$ the lengths of the zones and b_λ the instrumental broadening function. Since the LOS radiance depends uniquely on the product of the elemental densities and the zone lengths, we define the effective path of the first zone as

$$\overrightarrow{\widetilde{n}}_0 = \overrightarrow{n}_0 \cdot \Delta x_{zone_1} \qquad (2.4)$$

and in analogy to the relative concentrations in Eq. (2.2), we introduce the relative effective path $\overrightarrow{\widetilde{n}}_{rel}$ for the description of the effective path in the following zones. A simulated spectrum is thereby written as

$$\widetilde{I}_\lambda\left(F, \overrightarrow{T}, \overrightarrow{n}_e, \overrightarrow{\widetilde{n}}_0, \overrightarrow{\widetilde{n}}_{rel}\right) = F \cdot I_\lambda\left(\overrightarrow{T}, \overrightarrow{n}_e, \overrightarrow{\widetilde{n}}_0, \overrightarrow{\widetilde{n}}_{rel}\right) * b_\lambda \ . \qquad (2.5)$$

For the simulation of a spectrum in a two-zone approximation there will be $6 + K$ input parameters: one for the value of F, two for the value of the temperature, two for the electron density, one value for the relative effective path $\widetilde{n}_{rel}$, and K values for $\widetilde{n}_0$, where K is the number of elements in the plasma.

The atomic data necessary for calculating the plasma emission is taken from different sources. The electronic levels of the elements, their degeneracy and the Einstein coefficients of the electronic transitions are taken from the NIST database [12]. The Stark broadening and Stark shift parameters are taken mainly from the STARK-B database [13], evaluated with the contribution from free electrons only, and for a few selected lines of Mg, and Mn from the sources [14,15]. We did, however, not find the Stark parameters for all the relevant emission lines in our data. In such cases, the Stark shift is set to zero and the Stark broadening, which generally increases linearly with the electron density, is approximated by the linear function: $w_{stark}(n_e) = 0.05[nm]/1e23[m^{-3}] \cdot n_e$. The constant 0.05 was chosen such that the function produces values similar to the emission lines, relevant to this study, with known Stark broadening parameters.

3. Method for fits of simulated spectra

The goal of a fit is to find the values for the parameters $F, \overrightarrow{T}, \overrightarrow{n}_e, \overrightarrow{\widetilde{n}}_0$, and $\overrightarrow{\widetilde{n}}_{rel}$ that minimize the summed square residuals r^2 between the simulated intensities and the intensities of the input spectrum

$$r^2 = \sum_i\left(\left(\widetilde{I}_\lambda\left(F, \overrightarrow{T}, \overrightarrow{n}_e, \overrightarrow{\widetilde{n}}_0, \overrightarrow{\widetilde{n}}_{rel}\right)\bigg|_{\lambda=\lambda_i} - p_i\right)w_i\right)^2 \ , \qquad (3.1)$$

where $\widetilde{I}\big|_{\lambda=\lambda_i}$ is the simulated spectrum evaluated at the wavelength λ_i corresponding to the wavelength of the i'th bin and where p_i is the intensity of the i'th bin. The weight of the i'th residual is denoted by w_i.

In general $\widetilde{I}_\lambda$ is a non linear function, however, it increases monotonically with $\overrightarrow{\widetilde{n}}_0$. In the optically thin limit it increases linearly and the square residual r^2 can be minimized analytically in $\overrightarrow{\widetilde{n}}_0$ using the method of linear least squares. Even though the LIBS plasma is not optically thin

at all wavelengths, the above considerations indicate that the residuals of r^2 can be minimized semi analytically in $\widetilde{n}_0$ using non-linear least squares. Consequently, we choose to split the fit routine into two steps where the first steps tunes the parameters $\overrightarrow{T}, \overrightarrow{n}_e, \overrightarrow{n}_{rel}$ and the second step optimizes $\overrightarrow{\widetilde{n}}_0$ by non-linear least squares for different values of F. To reduce the problem further, fits are done to spectrally integrated peak intensities (groups of bins) instead of individual intensities, such that

$$r^2 = \sum_j\left(\left(\int_{\lambda_{j,min}}^{\lambda_{j,max}} \widetilde{I}_\lambda\left(F, \overrightarrow{T}, \overrightarrow{n}_e, \overrightarrow{\widetilde{n}}_0, \overrightarrow{\widetilde{n}}_{rel}\right)d\lambda - P_j\right)W_j\right)^2 \ , \qquad (3.2)$$

where P_j is the spectrally integrated intensity of peak j, W_j the weight of peak j and $\lambda_{j, min}$ and $\lambda_{j, max}$ the wavelength span of peak j. This reduction to a smaller number of peak intensities also has the advantage that it lowers the influence of several effects that change the spectral data: uncertain or unknown Stark parameters are less critical and the simulated intensities do not need to be convoluted with the instrumental broadening function b_λ (Eq. (2.5)). The limitation of this approach is that the information stored in the line profiles, e.g. the electron density through Stark broadening is not directly accessible anymore.

After the fit and for a better comparison of the residuals at the different fit parameter values, the residuals are normalized so that the residuals at the optimal solution is equal to the expectation value of the chi-square (χ^2) according to the degrees of freedom. As elements also contained in the atmosphere are not considered in the fit, fitted elemental concentrations and the reference values are normalized such that relative concentrations can be compared.

An overview of the steps of the fit routine is illustrated in Fig. 2 and the individual steps are explained in further detail below.

3.1. Pre-processing of input spectrum

The pre-processing of the input spectrum comprises identifying and extracting the spectral peaks and estimating their spectrally integrated intensities and weights. In order to identify peaks in the spectrum, a threshold is estimated from the trend line of the background spectrum and its noise. The trend line of the background is estimated using a moving minima method and its noise likewise but applied to the standard deviation of the intensities, calculated in smaller wavelength intervals. The threshold, for identifying the peaks, is chosen to be six times the spectral noise from the background. Peaks are then extracted by finding pixels with intensities above this threshold and tracing their neighboring pixels until the level of the background. With this approach no peak fitting is required and a peak might consist of several emission lines.
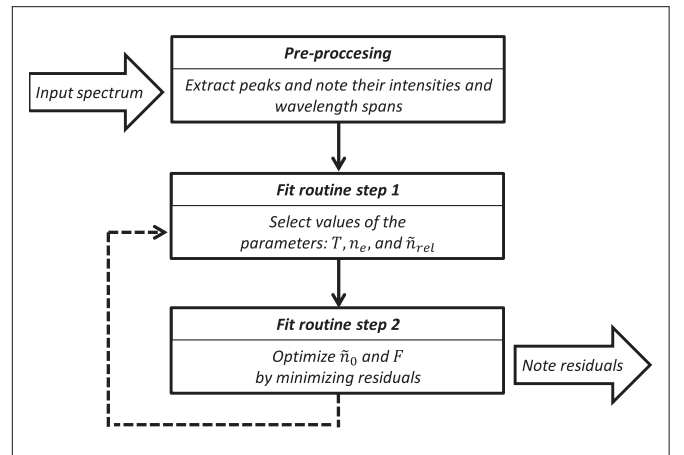

Fig. 2. Flow diagram showing the steps in the fit routine.

The intensity of a peak is calculated as the sum of the intensities of the bins making up the peak minus the background level

$$P_j = \sum_{i, \ \lambda_i \in P_j} p_i - p_{(bg),i} \ ,$$ (3.3)

where p_i is the intensity and $p_{(bg),i}$ the estimated background level at the i'th bin.

The weight of a peak is related to the uncertainty of its intensity and it is calculated as

$$W_j = \left(G \cdot P_j + \left(\sum_{i, \ \lambda_i \in P_j} \sigma_i^2 \right) + \left(0.05 \cdot P_j \right)^2 + \left(\sum_{i, \ \lambda_i \in P_j} \sigma_i \right)^2 \right)^{-1/2} .$$ (3.4)

Here, the first term contains the uncertainty due to counting noise, where G is the detector gain in counts per photoelectron. The second term contains the uncertainty due to the estimated spectral noise at the background level σ. The third term is a 5% peak uncertainty. It can be considered as a model uncertainty covering discretizations and uncertainties in the atomic constants and intensity calibration. The last term is added to weight the smallest peaks less since they are more prone to systematic errors in the estimation of the background level.

3.2. Fit routine

The optimization of the values for the parameters $\overrightarrow{T}$, $\overrightarrow{n}_e$ and $\overrightarrow{\widetilde{n}}_{rel}$ is done using the optimization method simulated annealing [16]. The possible values of the parameters are pre-determined and discretized by a set of parameter limits and parameter resolutions. The optimization method is a type of Monte Carlo method and only a limited and more relevant part of the parameter space will be visited as opposed to a full grid search. Given the set of values for $\overrightarrow{T}$, $\overrightarrow{n}_e$ and $\overrightarrow{\widetilde{n}}_{rel}$ from the previous step, optimal values of F and $\overrightarrow{\widetilde{n}}_0$ are obtained by minimizing the residuals, as given in Eq. (3.2), by non-negative non-linear least squares. In a loop over the extracted peaks, a system of equations between the spectrally integrated simulated intensities and the extracted peak intensities is arranged: 1

$$\int_{C_1} \widetilde{I}_\lambda \left(F, \overrightarrow{T}, \overrightarrow{n}_e, \overrightarrow{\widetilde{n}}_0, \overrightarrow{\widetilde{n}}_{rel} \right) d\lambda \cdot W_1 = P_1 \cdot W_1$$

$$\int_{C_2} \widetilde{I}_\lambda \left(F, \overrightarrow{T}, \overrightarrow{n}_e, \overrightarrow{\widetilde{n}}_0, \overrightarrow{\widetilde{n}}_{rel} \right) d\lambda \cdot W_2 = P_2 \cdot W_2$$

$$\vdots$$

$$\int_{C_k} \widetilde{I}_\lambda \left(F, \overrightarrow{T}, \overrightarrow{n}_e, \overrightarrow{\widetilde{n}}_0, \overrightarrow{\widetilde{n}}_{rel} \right) d\lambda \cdot W_k = P_k \cdot W_k \ ,$$ (3.5)

where C_k refers to the wavelength span of the k'th peak. There exists one equation for each extracted peak. Setting up the equations only requires the identification of peaks from the emission lines of the atmospheric elements that are not included in the fit. For the remaining peaks, no line identification is needed: all emission lines from our database with wavelengths within the wavelength spans of the peaks are included. In the optically thin limit, the simulated intensities are directly proportional to the product of $\overrightarrow{\widetilde{n}}_0$ and F. As a starting point, the equations are written in the optically thin limit and solved for $\left(\overrightarrow{\widetilde{n}}_0 \cdot F \right)$ using non-negative least squares. A first estimate of the instrumental factor F is then found from an initial guess of the sum of $\sum \overrightarrow{\widetilde{n}}_0 = \widetilde{N}_{guess}$ that are

related to the product of the total atomic density of the plasma and the zone lengths

$$F_{guess} = \frac{\sum \left(\overrightarrow{\widetilde{n}}_0 \cdot F \right)_{est.}}{\widetilde{N}_{guess}} \ ,$$ (3.6)

The parameter F is therefore related to the product of the density and length of the plasma. By setting F to F_{guess}, $\overrightarrow{\widetilde{n}}_0$ is decoupled from F and the system of equations, in the not optically thin limit, is linearized around the current values and an improved estimate of $\overrightarrow{\widetilde{n}}_0$ is obtained by again solving the equation. This process is repeated iteratively until convergence.

The experimental factor F was estimated from an initial guess of the total elemental density (Eq. (3.6)). The above process is therefore repeated for different values of F around the initial guessed value. The combination of F and $\widetilde{n}_0$, that resulted in the lowest residual, is saved and the residual is used for the selection of a new set of values for the parameters $\overrightarrow{T}$, $\overrightarrow{n}_e$, $\overrightarrow{\widetilde{n}}_{rel}$, for which the process is repeated.

The simulated peaks are evaluated with wavelength steps of 1/3000 nm and the derivatives in the linearization of the system of equations (Eq. (3.5)) are calculated numerically by the finite difference approximation.

4. Verification of method: fits to synthetic data

4.1. Synthetic test spectra

Three synthetic spectra were generated with an elemental composition equal to the carbonate sample (3.57 at.% of Ca, 5.44 at.% of Mg, 3.38 at.% of Mn, 12.68 at.% of Na, 18.73 at.% of C, and 56.20 at.% of O) from which the measured LIBS data was acquired (to be presented in Section 5.1). The first synthetic spectrum was created from a line of sight (LOS) with constant temperature and densities and will be referred to as the "Homogeneous" spectrum. The two other spectra were created from continuously varying profiles of the plasma properties discretized into twenty homogeneous zones. The used temperature profiles were those of a Gaussian and a shifted Gaussian function. These spectra will therefore be referred to as the "Gaussian" and "Shifted Gaussian" spectrum. The plasma properties along the LOS are shown in Fig. 3. Their values were chosen such as to provide similar values as the measured data in Martian atmospheric conditions when discretized in the two-zone model. This will be discussed further in the next section after the applications to the measured LIBS data. In order to mimic the measured LIBS data, the synthetic spectra were convoluted with the instrumental broadening function and integrated to fewer bins before Gaussian noise was added. The spectra span wavelengths from 273 nm to 800 mn and the signal to noise and number of detectable peaks are similar to that of the measured LIBS data (to be presented in 5.1). The resulting synthetic spectra can be seen in the supplementary materials.
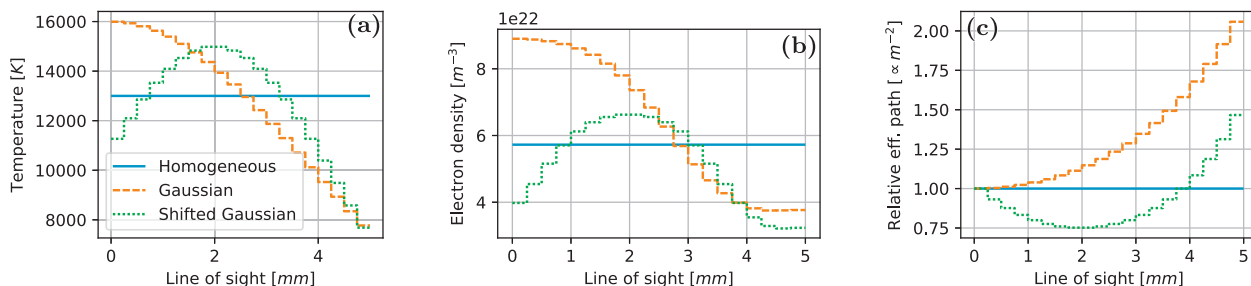
Fig. 3. The plasma properties of the synthetic spectra created to test the fit approach. (a) Temperature, (b) electron density, and (c) relative effective path.
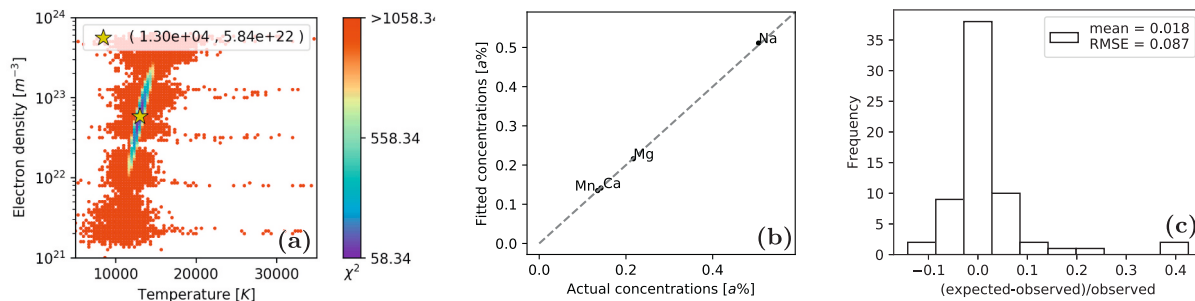

Fig. 4. (a) χ^2 for different values of temperatures and electron densities. The χ^2 has been normalized to the median value of its probability distribution. The best solution which is the only found minimum is marked by the star. (b) Fitted relative concentrations compared to the actual values. The relative deviations are within 1.1% and ascribed to uncertainties in the peak extraction due to the added noise. (c) Histogram of the residuals between the fitted and extracted peak intensities. Most residuals are within 5%, but peaks with larger residuals are also seen. These are the less intense peaks that are more affected by the noise in the spectrum.

4.2. One-zone model fit to "Homogeneous" spectrum

The results of the fit are summarized in Fig. 4. Fig. 4a shows the χ^2 for different values of the plasma temperature and electron density of the one zone model fit. White areas are parameters not visited during the optimization. The best fit is found for a temperature of 13,000 K and an electron density of 5.84e22 m^{-3}. The fitted temperature is equal to the true value and the fitted electron density value is the closest within the discretization of the parameter search space. The temperature appears more confined than the electron density and a positive correlation between the two properties is seen. The best solution is very well confined and only one minimum is observed. Fig. 4b shows the best fitted relative elemental concentrations compared to the true values. The relative deviations are within 1.1% and the concentrations appear to have converged correctly in the iterative solution of the linearised equations (Eq. (3.5)). Fig. 4c shows a histogram of the individual relative residuals between the fitted and observed peak intensities ((observed-fitted)/

observed). Most of the peak residuals are seen to be smaller than 5%, but residuals of around 40% are also observed. These higher residual values are for the less intense peaks that are more affected by the noise in the spectrum. These peaks are weighted less in the fit, according to Eq. (3.4).

4.3. Two-zone model fit to "Gaussian" spectrum

Fig. 5 shows the χ^2 for different values of the temperatures, electron densities and the relative effective path of the outer zone of the two-zone model. The best solution is found for a temperature of 14,000 K in the inner zone and a temperature of 8330 K in the outer zone (Fig. 5a) as well as an electron density of 6.92e22 m^3 in the inner zone and an electron density of 3.31e22 m^3 in the outer zone (Fig. 5b) and with a relative effective path of the outer zone of 55% (Fig. 5c). The fitted temperatures of the inner and outer zone are close to the average temperature $T_{avg} = 12,700$ K and the outermost temperature $T_N = 7800$ K, respectively, that are given by the temperature profile (Fig. 3). For the
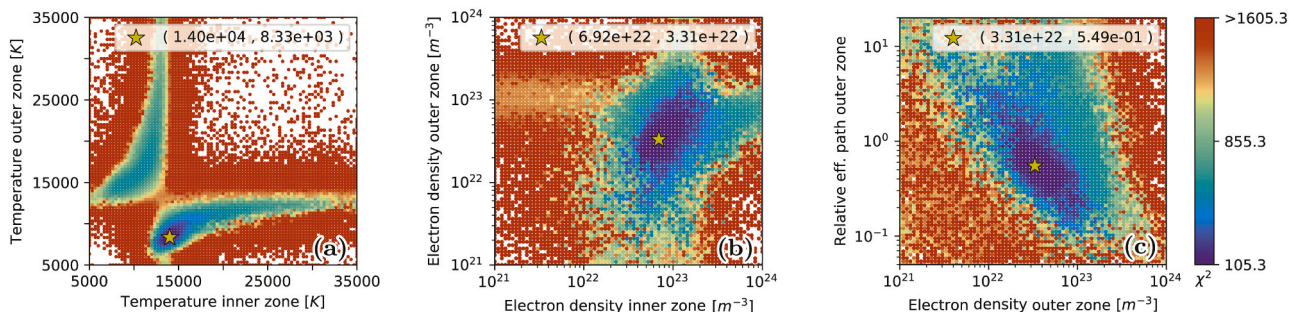

Fig. 5. Normalized χ^2 values for different values of the plasma model parameters shown for three different 2D projections using minimum intensity projection: (a) the temperatures of the zones, (b) the electron densities, and (c) the electron density and relative effective path of the outer zone. The Best solution is marked by the star. Everything above 1500 σ from the best solution is colored red. The best solution appears well confined in terms of sigmas, but another local minimum, with the properties of the zones interchanged, also appears. The two minima are separated by a χ^2 of ~500. (For interpretation of the references to colour in this figure legend, the reader is referred to the web version of this article.)
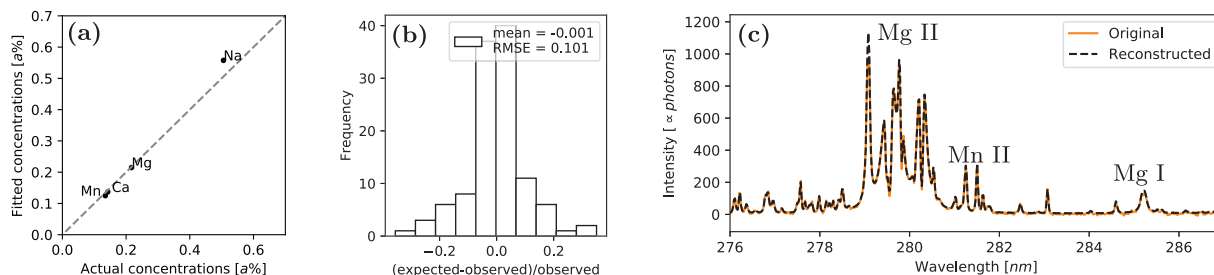
Fig. 6. (a) Fitted relative concentrations compared to the true values. The relative deviations are within 11%. (b) Residuals between the expected peak intensities and the observed peak intensities in the spectrum at the best fitted parameters. The residuals have a RMSE of 10% indicating a good description of the peak intensities in the fit. (c) Part of the reconstructed spectrum using the best fit parameters plotted together with the original data.

electron densities, the same pattern is observed but with the best fitted electron density of the outer zone being a little lower than at the end of the LOS. From the plot showing the residuals at different temperatures (Fig. 5a), a symmetry in the interchange of the zones can be seen. The symmetry results in a second local minimum with approximately the same values as the best fit, but with the outer zone being the hotter one. The two minima are well separated with a difference in χ^2 of ~500. The areas of low residuals around the two minima extend towards higher temperatures for one of the zones while approaching a value of T ~13,000 K for the other zone, indicating solutions in which the properties of one of the zones are more dominant than those of the other. The areas intersect at $T_{inner} = T_{outer} \sim$ 13,000 K, which is the one-zone solution for the Gaussian temperature distribution. Since the χ^2 value of this one-zone solution is more than 1100 sigma higher than that of the best solution, it is evident that a two-zone model could significantly improve the analysis of non-homogeneous plasmas.

For the best solution, the resulting concentration estimates, peak residuals and part of the reconstructed spectrum are shown in Fig. 6. The relative errors of the concentration estimates are within 11% (Fig. 6a) and the peak intensity residuals have a root mean square error (RMSE) of 10% (Fig. 6b). The reconstructed spectrum looks very similar to the original even in wavelength regions with superimposed and self reversed emission lines such as the strong Mg II lines at ~280 nm that can be seen in Fig. 6c.

4.4. Two-zone model fit to "Shifted Gaussian" spectrum

Fig. 7 shows the χ^2 for different values of the temperatures, electron densities and the relative effective path of the outer zone. The best solution is again found for values close to the average properties and the outermost properties (the values at the end of the LOS). For example, the best fit is obtained with a temperature of the inner and outer zone of 13,333 K and 8000 K, respectively. The average and outermost

temperature for this schedule is 12600 K and 7700 K, respectively (Fig. 3). The relative effective path of the outer zone obtained for the "Shifted Gaussian" is now smaller in comparison to the "Gaussian" and was found to be to 31% of that of the inner zone. The residuals for the different values of the plasma model parameters show the same patterns as the results obtained from the "Gaussian" spectrum. The symmetry in the interchange of the temperatures of the zones is seen from Fig. 7a and the resulting second local minimum, as well as the one-zone solution, are largely separated from the best solution in terms of χ^2 values.

The relative concentrations are estimated within 10% relative errors and the residuals of the peak intensities have a RMSE of 10%. The reconstructed spectrum from the best fit can be found in the supplementary materials and seen to match the original spectrum very well.

4.5. Discussion

The "Homogeneous" spectrum was created from constant values of the plasma properties along the LOS which corresponds to a one-zone plasma model. The fit of the one zone-model to the "Homogeneous" spectrum is thereby an example of fit model and data correspondence. The outputs from this fit were therefore expected to be very similar to the original data. The results meet this expectation and validate the process of iterative linearisation and solving of the system of equations between the peak intensities (Eq. (3.5)). The smaller deviations in the peak intensities and elemental concentrations are explained by uncertainties in the peak extraction due to the added noise.

The results for the "Gaussian" and "Shifted Gaussian" spectra confirm that plasmas with variations of the plasma properties are well approximated by a two-zone model. This is seen by the small deviations in the concentration estimates, the peak residuals, and by eye when comparing the reconstructed spectrum to the original data (Fig. 6). The difference between the observed and fitted peak intensities has a RMSE of ~10% for both cases. This is comparable to the RMSE of the peak

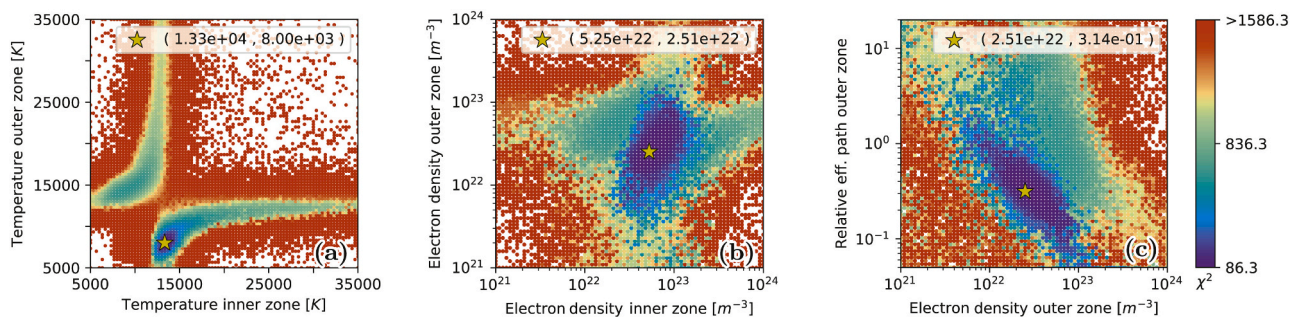**Fig. 7.** Normalized χ^2 for different values of the plasma model parameters shown for three different 2D projections using minimum intensity projection. (a) the temperatures of the zones, (b) the electron densities, and (c) the electron density and relative effective path of the outer zone. The best solution is marked by the star. Everything above 1500 σ from the best solution is colored red. (For interpretation of the references to colour in this figure legend, the reader is referred to the web version of this article.)

intensities from the one-zone fit to the "Homogeneous". The RMSE of the peak intensities can therefore largely be ascribed to uncertainties in the process of determining the observed peak intensities and the contribution to the RMSE from the discretization into a two-zone model therefore seem small. Adding a third zone to the fitted model would therefore not improve the results significantly. In fact, the peak residuals are lower than the intensity variation that is expected for many of the relevant emission lines due to the uncertainties in the Einstein coefficients found in the literature (up to 50% relative uncertainties with 90% confidence intervals) [12].

The best fitted values of the temperatures and electron densities of the inner and outer zones are close to the average values and the values at the outermost simulated plasma region, respectively. An interpretation of this is that the first zone represents the bulk emission, which is well described by averaged properties, while the second zone is more important for the description of the absorption, which is well described by the outermost temperature. This interpretation is motivated by considering the optically thick limit where the spectrum would be described by the blackbody spectrum with the outermost temperature. The simulated profiles for the synthetic spectra do not lead to a completely optically thick plasma, but the surface/outermost temperature is still important for the description of the absorption. This implies that the significance of a second zone becomes larger with increasing

absorption in the laser-induced plasma. The effect of absorption is also what distinguishes the two observed local minima with similar but interchanged values of the properties of the zones. In the case of negligible absorption, the order of the zones would not matter since all the emitted light would reach the detector without any absorption. In the case of non negligible absorption, the order of the zones becomes significant.

5. Analysis: fits to real data obtained in Martian atmospheric conditions

5.1. Experimental set-up

The LIBS system at the German Aerospace Center (DLR) in Berlin was used for all measurements presented in this study. The set-up uses a Q-switched Nd:YAG laser with a wavelength of 1064 nm, a pulse length of 6 ns and maximum output energy of 220 mJ per pulse. The output energy can be adjusted by inserting different combinations of neutral density filters in the laser beam path.

The plasma emission is captured in a top view configuration with a toroid mirror reflecting the plasma emission onto the slit of an echelle spectrometer (LTB Aryelle Butterfly). The spectrometer is equipped with an ICCD (Andor iStar) detector which allows for time-resolved
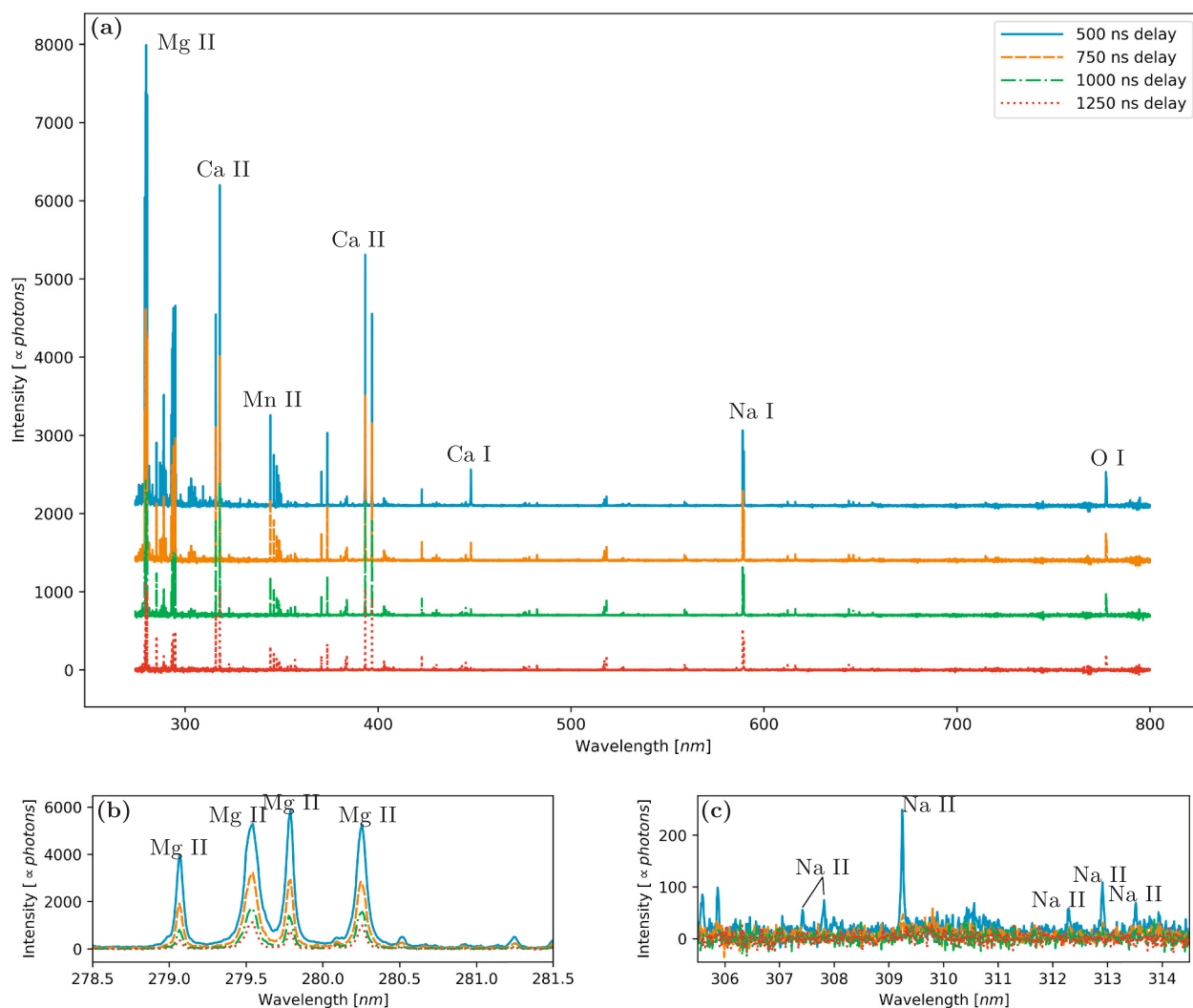

Fig. 8. The median spectra of the carbonate mixture at the four different delay times. (a) full spectral range and shown with an offset, (b) close-up of the strong Mg II emission lines and (c) close-up of several Na II lines from highly excited states ~37 eV.

measurements and has a fill factor close to 100%. The UV-VIS-NIR configuration of the spectrometer covers a spectral range from 270 nm to 850 nm, in ~29,000 bins, wherein the instrumental broadening is well described by a Gaussian with a full width at half maximum varying linearly from 0.033 nm at 270 nm to 0.082 nm at 850 nm. The samples are placed in an air tight chamber that can be evacuated and subsequently filled with Mars-analog gas (consisting of 95.55 vol% of CO_2, 2.7 vol% of N_2, 1.6 vol% Ar and 0.15 vol% O_2) to simulate Martian ambient conditions. The field of view of the spectrometer is approximately 0.5 mm × 0.5 mm in the focal plane and has an acceptance angle of ~3°. The relative intensity response has been determined using a calibrated broadband light source.

5.2. Measurements

For the LIBS measurements a sample mixed from different carbonates was prepared. Pure powders of $CaCO_3$, $MgCO_3$, $MnCO_3$ and $Na2CO_3$ were grounded and mixed in a mortar before being pressed into a small pellet of 1 g by applying 5 tons for 10 min. The elemental concentrations in the sample are 3.57 at.% of Ca, 5.44 at.% of Mg, 3.38 at.% of Mn, 12.68 at.% of Na, 18.73 at.% of C, and 56.20 at.% of O. The uncertainties of the concentrations due to weighing of the powders are below 0.05 at. %.

All the LIBS measurements were performed in simulated Martian atmospheric conditions. The pressure in the air tight chamber was balanced by in- and outflow to be stable at ~7 mbar.

Measurements were taken with a gain of ~6 counts per photoelectron with a fixed integration time of 50 ns at four different delay times: 500 ns, 750 ns, 1000 ns and 1250 ns. The laser energy was attenuated to be 35 mJ as measured at the sample surface and operated at a frequency of 10 Hz. The light emitted by 30 sequentially laser-induced plasma plumes was integrated to obtain one LIBS measurement. For each delay time, the sample was measured at eight different positions and four repetitions per position. The first measurement at a new position was generally found to vary strongly from the subsequent measurements at that same position, so that these were considered to be cleaning shots

and were therefore discarded. Of the remaining 24 measurements (30 · 24 laser pulses) for each delay, a single median spectrum was calculated to obtain a good signal-to-noise ratio. The median spectra with the intensity calibration applied are shown in Fig. 8. The spectra contain very little continuum emission and the intensity is seen to decrease with increasing delay time.

5.3. Two-zone model fits to measured spectra

The χ^2 for different plasma model parameters are shown in Fig. 9 for the spectra at 500 ns and 750 ns delay times. The same symmetry as for the synthetic test spectra is seen in the residuals of the temperatures and the symmetric solutions with similar but interchanged values of the zones are also local minima separated by ~25 χ^2 values for both times. The one-zone solutions found at $T_{inner} = T_{outer}$ around 15,000 K and 13,000 K for 500 ns and 750 ns delay, respectively, can also be seen in Fig. 9. They are both separated by ~100 χ^2 values from the best solutions. At the one zone solution two lines of solutions with similar residuals can be seen. The lines are given by constant temperatures of either of the zones. For the residuals at 500 ns delay (Fig. 9a), following the line of constant temperature for the outer zone a third local minimum can be vaguely seen at temperatures of the inner zone of ~ 35,000 K. The χ^2 for this minimum is still much higher than for the global minimum. Nonetheless it might indicate the existence of a higher temperature component of the plasma for describing some of the observed peaks in the spectrum. This local minimum is not seen in the χ^2 plots for the spectrum at 750 ns delay (Fig. 9b). The structures of the χ^2 plots for the spectra at 1000 ns and 1250 ns delay are similar to the one for 750 ns delay and they are therefore not shown here but can be found in the supplementary materials. The plasma properties from the best fits and their uncertainties as a function of delay time are summarized in Fig. 10. The $\pm 3\sigma$ confidence intervals of the properties are indicated by the vertical bars. The confidence intervals were estimated, with correlations, by reading of the widths of the χ^2 contours at $+3\sigma$ from Fig. 9. In general, the uncertainties are asymmetric and the properties are strongly correlated. The temperatures are better constrained than the electron
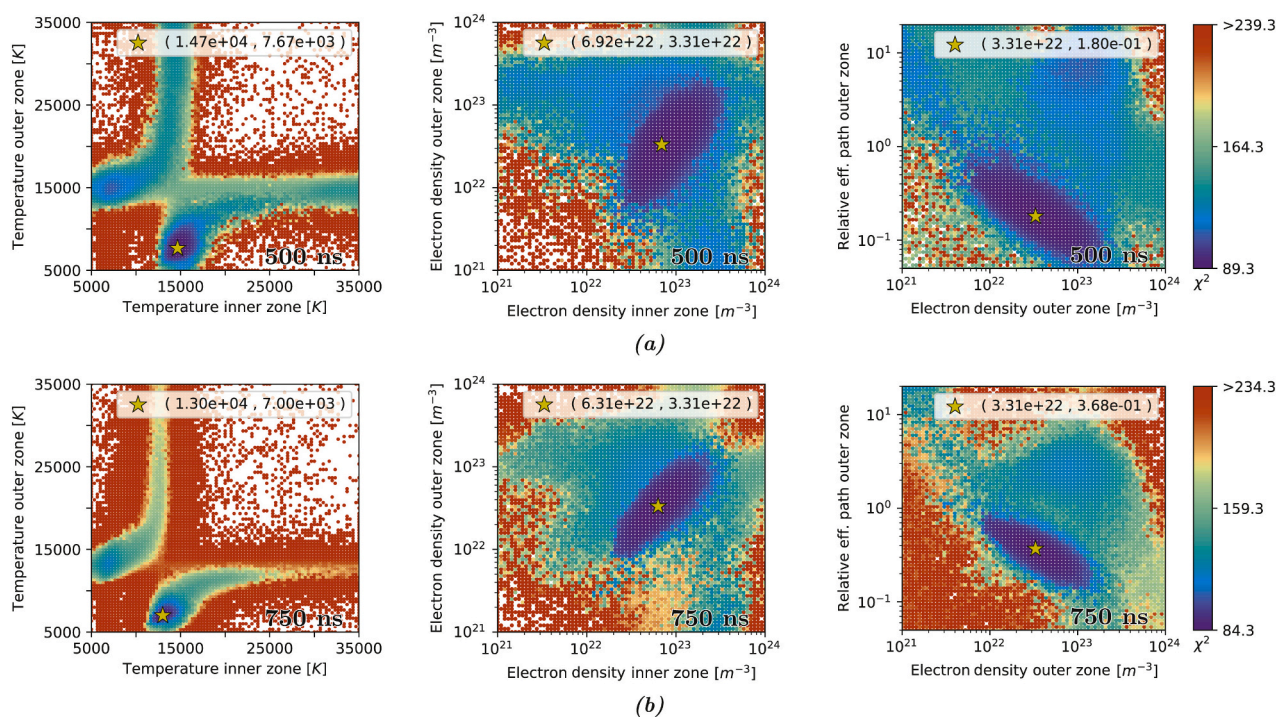

Fig. 9. Normalized χ^2 values for different values of the plasma model parameters shown for three different 2D projections using Minimum intensity projection. (a) Spectrum at 500 ns delay and (b) spectrum at 750 ns delay.
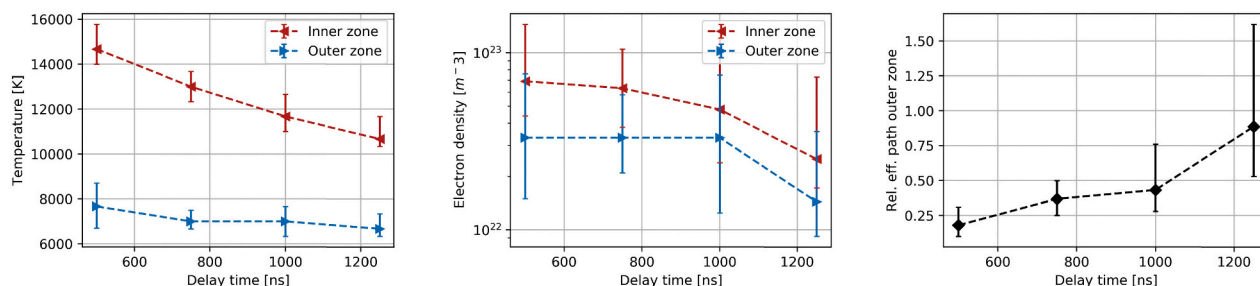
Fig. 10. Temporal evolution of the fitted plasma model parameters and their uncertainties ($\pm 3\sigma$). The temperatures of both zones are seen to decrease with increasing time. The same is true for the electron density of the inner zone. The electron density of the outer zone remains constant until 1000 ns from where it decreases with a factor ~2. The relative effective path of the outer zone increases monotonically with time.
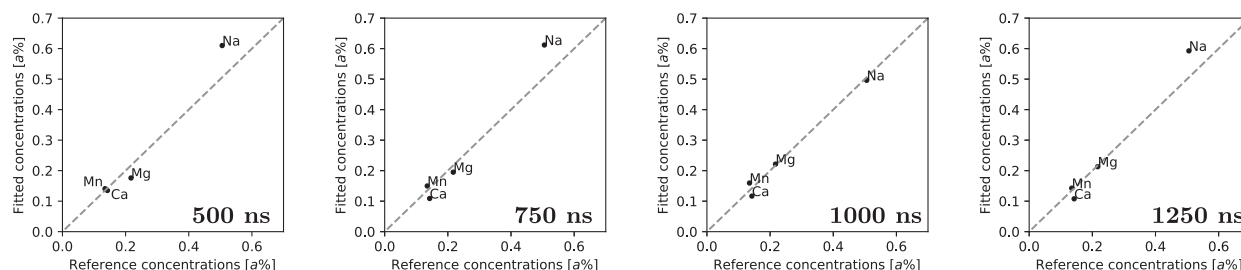

Fig. 11. Fitted relative concentrations plotted against the reference concentrations. The relative errors are within 25% for all elements at all the considered delay times.
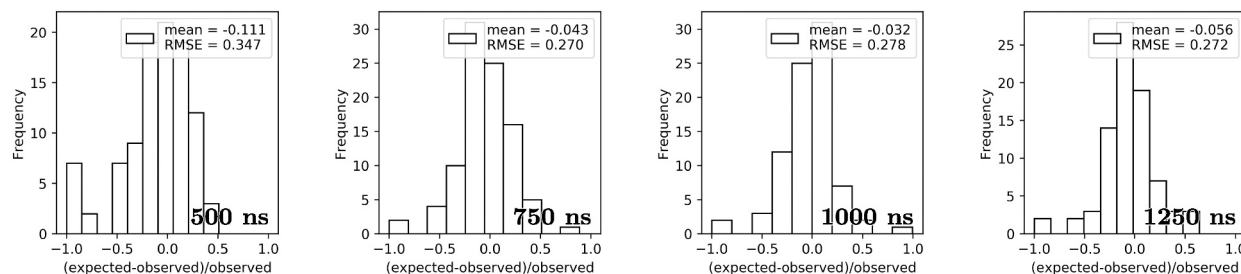

Fig. 12. Histogram of the residuals between the expected peak intensities and the observed peak intensities in the spectrum. The RMSE and the mean of the distribution are noted in the legends. The residuals at 500 ns delay are strongly affected by seven peaks that are not described in the fit at all. Omitting these the residuals would have a RMSE similar to the values at the later times.

densities and the relative effective path of the outer zone. As expected from a cooling of the plasma, the temperature decreases with time. This is also the case for the electron density of the inner zone, whereas the electron density of the outer zone remains constant until 1000 ns and then drops. Finally, the relative effective path of the outer zone is seen to rise monotonically with time, starting from about 20% of that of the inner zone at a time of 500 ns and growing to 90% at 1250 ns.

The resulting concentration estimates are shown in Fig. 11. Uncertainties have not been derived from the fit, but the relative deviations from the reference values (the values obtained from the mixing of the sample) are within 25% for every element at all delay times. Histograms of the peak residuals at the optimum solutions are shown in Fig. 12. At 500 ns the RMSE of the residuals is around 35%, but the number is strongly influenced by seven peaks in the spectrum that are not explained in the fit at all (leftmost bin in historgram of Fig. 12a). These peaks will be discussed later. Ignoring them, the RMSE would be around 25% which is similar to the values of the later delay times.

For the delay time of 500 ns, the reconstructed spectrum is shown together with the measured spectrum in Fig. 13. The reconstructed spectrum mostly matches the measured spectrum well. An exception is

the relatively weak emission lines shown in the close-up with wavelengths from 309 nm to 322 nm (Fig. 13c). These emission lines are identified as Na II transition from the high upper electronic level of 37 eV. These lines constitute most of the peaks with zero expected intensity that are seen in the left most bin in the histogram for the peak residuals (Fig. 12a). Their high upper electronic level suggest a high temperature and they are most likely the emission lines causing the local minimum at ~35,000 K seen in the χ^2 plot for different temperatures of the zones (Fig. 9a). In the wavelength range from 613 nm to 652 nm, another example of a discrepancy between the measured and reconstructed spectrum can be seen. Here, a Mg II line with significant intensity is seen in the reconstruction where no peak is observed in the measured spectrum. Since the fit is done to the observed peaks only, the χ^2 is not affected by this line. If it was, it would likely pull the temperature of the inner zone towards a lower temperature due to the relatively high upper electronic level of the emission line (14 eV). In the close-up showing the wavelengths from 344 nm to 350 nm, some Mn II lines can be seen. These show a shift in wavelengths between the measured and reconstructed spectrum. This is most likely due to changes in the wavelength calibration of the LIBS set-up, but could also be due to a large Stark shift.
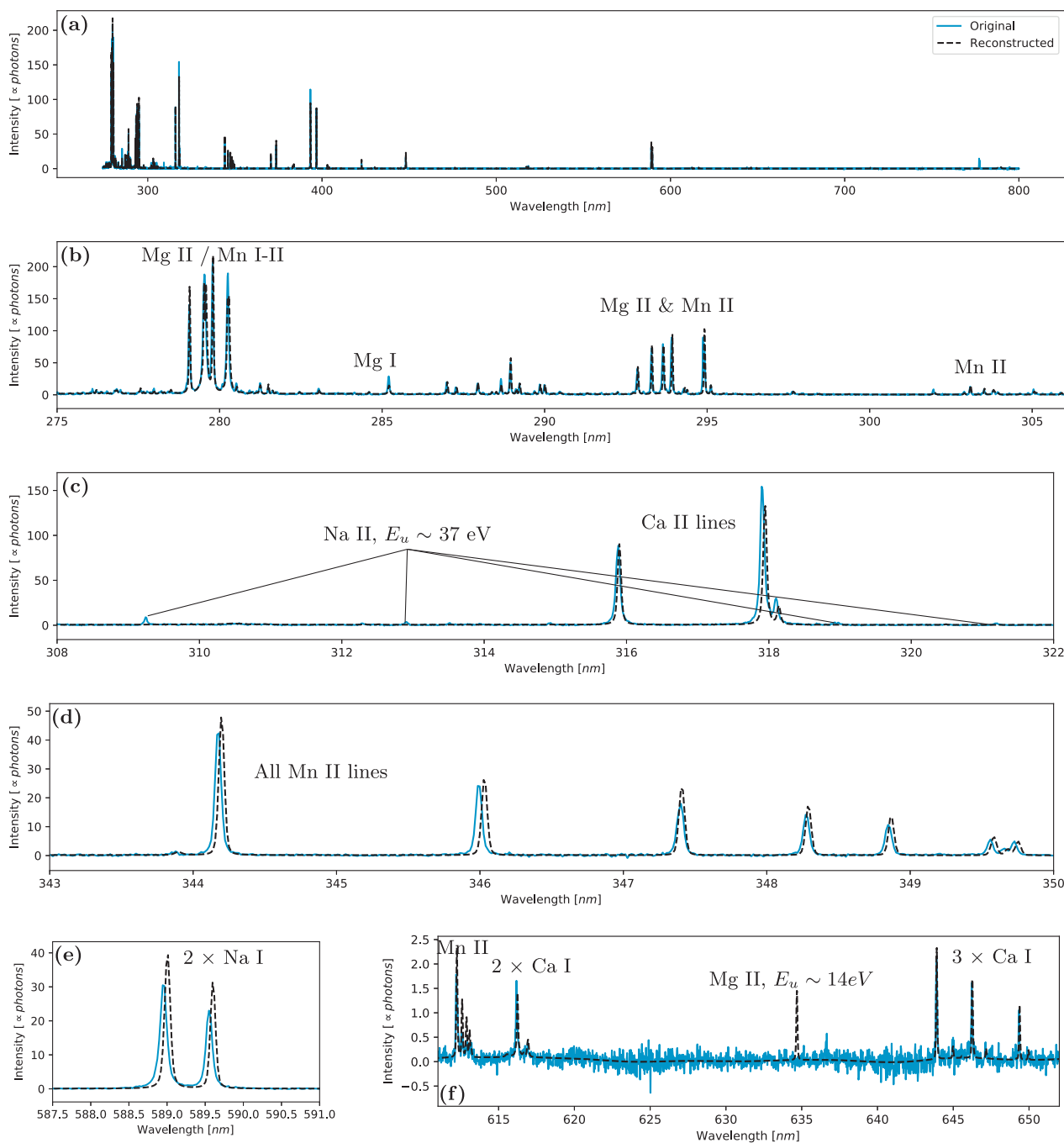
Fig. 13. Reconstructed spectrum at 500 ns delay using the best fitted parameters plotted together with the measured data. (a) the full spectral range and (c)-(f) close-ups including smaller wavelength ranges. Most line intensities are modeled well in the fit, but some discrepancies such as the Na II lines in (c) and the Mg II line in (f) are also observed.

Such shifts are observed for many of the emission lines, however they are not directly affecting the fit since only integrated peak intensities are considered. This illustrates the robustness of the approach.

The reconstructed spectrum at 1000 ns delay is shown together with the measured spectrum in Fig. 14. At this longer delay time, the highly excited Na II emission lines are not seen any longer in the measured data. This is in agreement with disappearance of the high temperature local minimum in the χ^2 plots for the temperatures (Fig. 9). As most other emission lines seem slightly better described at this delay time (Fig. 12), the Mg I resonance transition at 285 nm is now worse described and is fitted to approximately half of the observed intensity

(Fig. 14). The Einstein coefficient of this line has a low uncertainty (3% with 90% confidence intervals) and the reason for the discrepancy must be found elsewhere. In the fit, this Mg I line is predicted to be strongly self-absorbed and saturated at the blackbody value of the temperature of the outer zone. An increase in the temperature of the outer zone is therefore likely to improve the description of this line. The comparison of the reconstructed spectra to the measured at 1250 ns delay and 1500 ns delay are similar to the one at 1000 ns delay and are therefore not shown. They can be found in supplementary materials.

Using the best fitted parameters, the pixel intensities as measured by this particular LIBS set-up have been predicted and compared to the
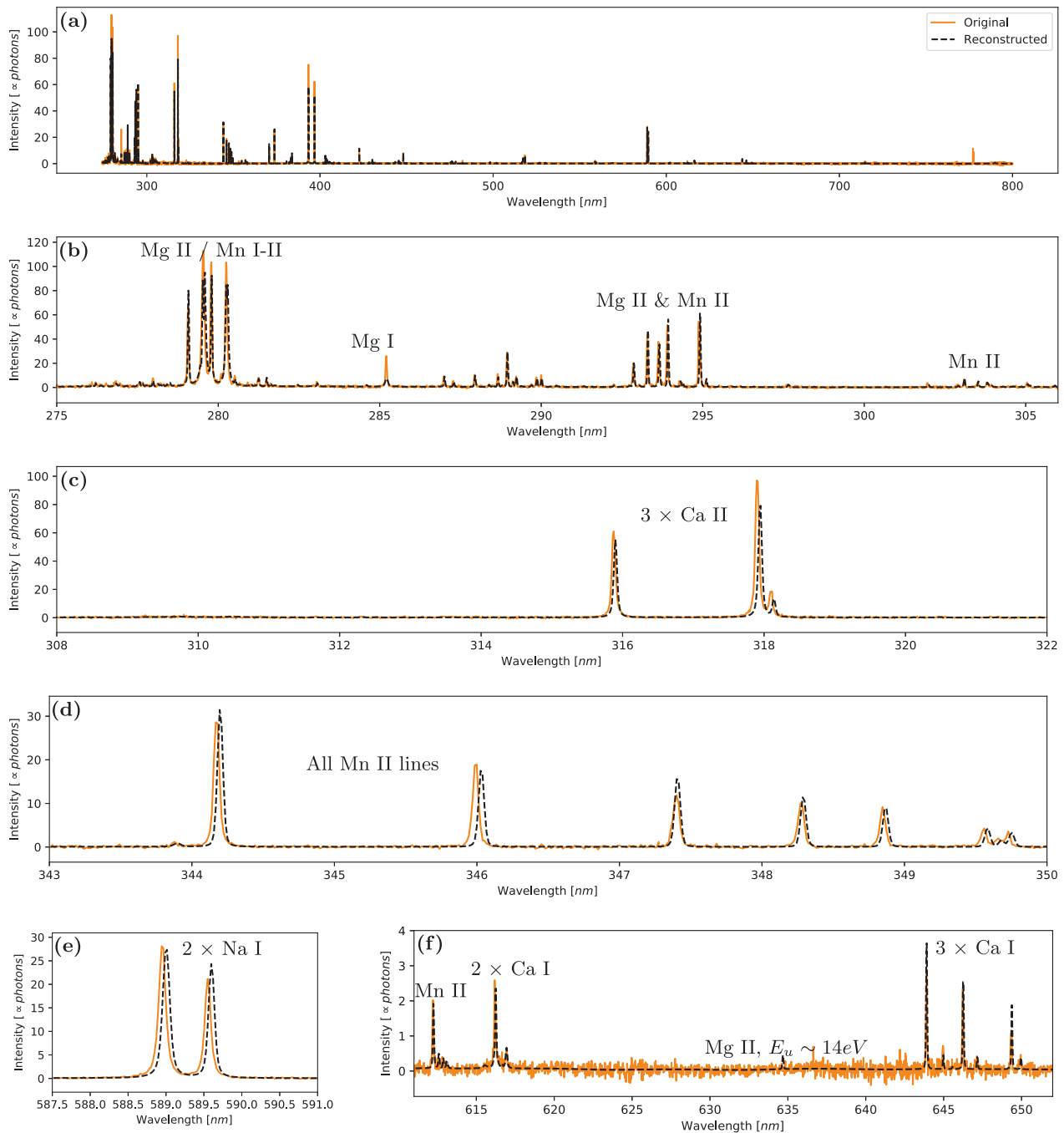
Fig. 14. Reconstructed spectrum at 750 ns delay using the best fitted parameters plotted together with the measured data. (a) The full spectral range. (b-d) Close-ups of smaller wavelength ranges. Most of the lines causing the larger discrepancies observed in the spectrum at 500 ns delay are now no longer visible in the spectra. The Mg I resonance transition at ~285, however, is now significantly underestimated in the fit as seen from (b).

prediction when omitting the process of absorption. The results are shown in the histograms of Fig. 15. It can be seen that absorption is predicted to affect the spectra strongly at all the considered delay times. As an example, it is seen that absorption reduces the strongest pixel intensities by almost two orders of magnitudes.

To asses the validity of the assumption of LTE, the decay time ($T/(dT/dt)$, $n_e/(dn_e/dt)$) and the characteristic variation length ($T/(dT/dx)$, $n_e/(dn_e/dx)$) of the temperature and electron density have been evaluated from the temporal evolution of the fitted plasma properties (Fig. 10). The decay time was calculated by considering the derived plasma properties at the earliest and latest times. The characteristic

length was calculated by averaging the properties of the inner and outer zone over the four different delay times assuming a total length of the plasma of 4 mm. The values can be seen in Table 1. For the possible existence of LTE, the decay time should be larger than the relaxation time for the excitation of the excited states and characteristic length should be larger than the particle diffusion length during the relaxation time. Furthermore, the electron should be sufficiently high so that excitation are dominated by collisions and the loss of excitation from radiative processes, due to optically thin conditions, can be assumed negligible. This last criteria is known as the McWhirter criteria. Following the approach in [5] and the approximate formulas given
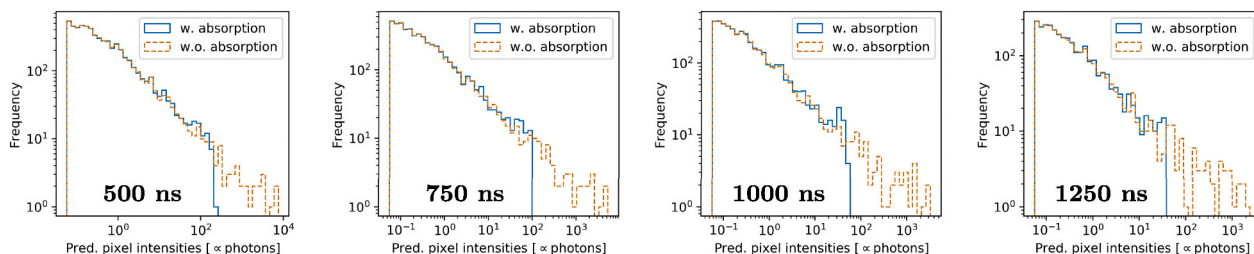
Fig. 15. Predicted pixel intensities with and without the effect of absorption. The intensities have been predicted using the best fitted parameters. Absorption is seen to strongly affect the intensities. The maximum pixel intensities for example are almost two orders of magnitude larger when omitting the effect of absorption.

Table 1
Decay time and Variation length calculated from the fitted plasma properties shown in Fig. 10.

	Decay time inner zone [ns]	Decay time outer zone [ns]	Variation length [mm]
Temperature	2300	5300	14
Electron density	870	1100	14

therein, the relaxation time, the diffusion during the relaxation time, and the McWhirter criterion have been calculated for the elements used for the fit (calcium, magnesium, magnesium, and sodium) and additionally for oxygen. The results are shown in Table 2. From comparing the values in the two tables it can be seen that the criteria for the assumption of LTE are not violated for Ca I-II, Mg I-II, Mn I-II, and Na I, whereas all the criteria in both inner and outer zone are violated for Na II and O I-II. This will be addressed later in the following section.

5.4. Discussion

When observing the χ^2 plots for the different plasma model parameters, at least two local minima are observed for all times. The symmetric solution, i.e. the solution where the best fitted parameters of the zones are interchanged, is for all spectra a second local minimum. Nonetheless, the minima observed in the temperatures are well confined and the temperature is by far the most important parameter in the thermodynamic description of the plasma. The electron density values and the relative effective path of the outer zone are not equally well confined and the uncertainties are bigger. This can also be seen in the χ^2 plots for the synthetic test spectra. The explanation for this is that the electron density only slightly changes the degree of ionization compared to the temperature. And as only integrated intensities are considered, the information about the electron density from the line profiles is not directly utilized in the fits which otherwise could help further confine the electron density presuming accurate values for the Stark broadening, Stark shift, and a proper wavelength calibration of the LIBS set-up.

For the considered delay times, the criteria for the assumption of LTE are only violated for Na II out of the considered species in the fits (Tables 1 and 2). In line with that, the general impression is that the two-zone fits describe the measured data well. As inferred from the one-zone solution, contained in the two-zone model, the step from a one-zone model to a two-zone is significantly improving the description of the time resolved LIBS data in Martian atmospheric conditions. For completeness, the method of multi-element Saha-Boltzmann plots has also been applied to the measured data. The results can be found in the supplementary materials. The resulting temperature estimates are similar to the fitted values of the inner zone, but the deviations between the estimated relative concentrations and the reference values are larger than the values obtained via the two-zone model. Besides the assumption of an optically thin plasma, the method of Saha-Boltzmann plots assumes a homogeneous plasma. From the fits of the two-zone model, it can be inferred that the outer zone, with the lower temperature, is most important for describing the absorption of the emissions from the already emitted light, and only adds little to the intensities of the optically thin emission lines from transitions involving the lower lying excited atomic states. Saha-Boltzmann plots can thereby probably provide equally good concentration estimates, as the ones of the two-zone model, when selecting the emission lines carefully in terms of negligible self-absorption and similar electronic and ionization energies. In this study, the only observable Sodium lines, besides the non-equilibrium Na II lines, are not optically thin and in order to derive good concentration estimates for sodium, a two-zone model would be preferable.

In the two-zone fits, the observed intensities are described with a RMSE of 35% for the spectrum at 500 ns, and within 28% for the later times. Furthermore, the reconstructed spectra match the measured spectra well, but with a few exceptions such as the peaks from emission lines involving highly excited states of Na II visible in the spectrum at 500 ns delay and the underestimation of the Mg I resonance transition at 285 nm for the later delay times. In the thermodynamic description of the atomic states, a very high temperature is required in order to populate the upper electronic levels (~37 eV) involved in the transitions for the observed Na II. This was also indicated by the hight temperature

Table 2
McWhirter criterion, relaxation time and the Diffusion during relaxation time calculated using the averaged fitted plasma properties of Fig. 10 and the approximate formulas in [6] assuming a fully ionized plasma. The values can be compared to the fitted electron density, the plasma decay time and the characteristic length variation (Table 1) in order to assess the validation of the assumption of LTE.

	Inner zone			Outer zone		
	McWhirter	relaxation	Diffusion during	McWhirter	relaxation	Diffusion during
	Criterion [m^{-3}]	Time [ns]	Relaxation time [mm]	Criterion [m^{-3}]	Time [ns]	Relaxation time [mm]
Ca I	4.5e21	0.5	0.09	3.4e21	5.9	0.3
Ca II	5.5e21	1.1	–	4.1e21	14	–
Mg I	1.5e22	2.9	0.68	1.1e22	86	1.5
Mg II	1.6e22	0.95	–	1.2e22	30	–
Na I	1.7e21	0.47	0.12	1.3e21	3.0	0.29
Na II	6.6e24	2.9e13	–	5.0e24	7.5e23	–
O I	1.5e23	2700	33	1.6e23	3.1e7	1100
O II	5.9e23	6.8e5	–	4.4e22	3.5e10	–

local minima in the χ^2 plots for the plasma properties of the zones at 500 ns delay. But such hotter zone would inevitably also affect the intensities of the other emission lines that are already well described by the best fitted, and more moderate temperatures values. Therefore, the Na II emission lines are more likely better modeled by non-equilibrium effects instead of a third hotter layer. The nature of the non-equilibrium should not be attributed to the violation of the McWhirter criterion since no excited states of Na II are supposed to be populated at the inferred temperatures. To give another example, Ca III would not satisfy any of the criteria of LTE, but that is not a problem since no Ca III ions exist at the considered delay times. The observation of the Na II lines is therefore most likely due to the combination of the recombination character of the plasma and a relatively long recombination rate of Na III. In the beginning of the plasma lifetime, Na III ions probably exist due to the high temperatures and if the recombination rate is around 500 ns or larger, the highly excited states of Na II could still appear after 500 ns due to recombination cascades. For comparison, the recombination time of Ti II was estimated in [17] to be around 1e-7 s to 1e-6 s, in a laser induced plasma in a low-pressure environment. However, the species out of equilibrium such as the Na II may have negligible abundance, and the LTE model still provides an accurate description of all other species and results in good concentration estimates, even for sodium.

When comparing the results to the results from the synthetic "Gaussian" and "Shifted Gaussian" spectrum it can be seen that the fitted model parameters of the zones are similar. This indicates that the true profiles of the measured data could have similar gradients as the true profiles of the synthetic spectra. Since the emission lines are modeled well in the fits to the synthetic spectra, the poor description of the Mg I line cannot be ascribed to the discretization of a two-zone plasma model.

For the synthetic spectra the relative deviations in the concentration estimates are within 11%. This number can be used as an lower limit of the expected uncertainties for applications to real data. For the real spectra, the relative deviations in the predicted concentration are within 25% relative errors and thereby not far from the expected uncertainties. When considering the different physical characteristics of the elements in the sample, concentration estimates within 25% errors seem convincing. For an example, Na I has as ionization energy of 5.14 eV whereas that for Mg I is 7.65 eV and the atomic weight of Mn is more than twice as that of Na. These are characteristics that make the concentration estimates more dependent on a correct description of the plasma properties due to different degrees of ionization but also challenge the assumption of equal elemental distributions in the plasma due to different expansion velocities. In [18] the latter effect was studied for hydrogen and deuterium in a plasma induced in argon at 5 mbar. They found that the relative measurement error due to this effect increases with time and can reach 50%. For this study, the effect seems smaller due to the consistency in the concentration estimates with time. This might be due to the higher laser energy used here (35 mJ versus 5 mJ).

As there are multiple sources for deviations between the measured and the modeled data (experimental uncertainties, uncertainties in the atomic constants, and plasma model assumptions), deviations in the predicted elemental concentrations and in the description of individual emission lines such as the Mg I transition at 285 nm are expected.

From the two-zone fits to the synthetic spectra, it was observed that the parameters of the inner zone adapts to values close to the average plasma properties and the parameters of the outer zone adapts to values close to the properties at the end of the LOS. With this in mind, the average plasma and surface temperature is likely to be a good interpretation of the fitted parameters of the real data. In the study of Hermann et al. [19], it was found that the LIBS plasma induced in an Argon atmosphere at a pressure of 500 mbar, at certain experimental conditions, produces an almost homogeneous plasma core containing target material and with all the temperature gradients in the background argon gas. It was argued to be due to the isolating properties of Argon (mostly elastic collisions with elements from target materials due to large spacing between ground and first excited state of Ar I). The thinner

Martian atmosphere at ~7 mbar pressure of mainly CO_2 is likely to be less isolating, and indeed gradients in the plasma properties are evidenced by the differences of the fitted parameters of the inner and outer zone (Fig. 10). The fitted electron density values of this study are furthermore relatively low compared to estimates from measurements in thicker atmospheres. Hermann et al. [10] found that the electron density in the laser plasma of an aluminium target in Earth's atmosphere at a delay time of ~1000ns is about 5e23 m^3 whereas the electron density at 1000 ns was estimated to be 3.31e22 m^3 in this study. The measurements in Earth's atmosphere were done with an UV laser with a 4 ns pulse length and 6 mJ pulse energy. The pulse energy used for the measurements in this study was 35 mJ, but still the electron density is approximately an order of magnitude lower. As pointed out in [4] this is due to the lower pressure of the Martian atmosphere that allows the induced plasma to expand into a larger volume. This also makes the LIBS plasma in Martian atmosphere decay faster than in thicker ambient atmospheres due to an increased cooling due to expansion. Furthermore, it decreases the effect of self-absorption which was already found to strongly affect the pixel intensities in the spectra of this study. Even though the plasma in Martian atmospheric conditions is decaying faster and less dense than plasmas induced in higher pressures, the plasma properties were found to be consistent with the approximation of the assumption of LTE for all the considered species except of Na II. When including non-metallic species, such as oxygen or carbon, the criteria for LTE would not be fulfilled (see Table 2 for oxygen). In general LTE is favored when the electron density is increased, and it might be that an increasing laser energy could result in a sufficient increase. Another approach would be to go to even earlier delay times where the plasma would be denser, but as other non-equilibrium effects were discovered at the delay time of 500 ns in terms of the Na II emission lines, this is probably not favorable. As the considered criteria for LTE refers to the set of levels that are the most difficult to retain in or establish to equilibrium, i.e. the ground state and the first stable excited state. Higher excited states of such non-metals will probably be in equilibrium (due to the decreasing spacing between higher excited levels). The plasma properties for describing the metals might therefore also provide a good description of the emissions of non-metals which could be included in the spectral modeling. The non-equilibrium effects would then be expressed by errors in the concentration estimates, due to the non-equilibrium of the ground state, but the emission might still be well modeled. This would be interesting to investigate in a follow-up study.

6. Conclusion

A fit routine for fitting a two-zone plasma model to time resolved LIBS spectra obtained in Martian atmospheric conditions has been implemented. The fit routine works by simulating the observed and integrated peak intensities from a one-dimensional LTE model and tuning the model parameters in a two step fit routine. The outputs from a fit are the plasma temperature and electron density in the approximation of a one- or two-zone plasma model, the elemental concentrations, and the corresponding line identification. The fit routine has been applied to both synthetically generated and experimentally measured time resolved LIBS data of a pellet of mixed carbonates measured in simulated Martian atmospheric conditions. The method is calibration-free and could in principle be applied to any sample consisting of elements with available atomic data, but special care must be given to the recombining nature of the plasma at early delay times (observed at delay 500 ns) and non-metallic elements due to non-fulfillment of the LTE criteria as given in [5]. However, the criteria seem to be fulfilled for most metals under the considered experimental conditions.

The results from applications to synthetic data show that spectra simulated from line of sights with large gradients in the plasma properties can be approximated well by a two-zone plasma model with the inner and outer zone adapting to approximately the average plasma properties and the properties at the end of the line of sight, respectively.

When fitting a two-zone model to measured LIBS data, the concentration estimates are within 25%. Despite smaller discrepancies between the measured and fitted spectra, the two-zone LTE plasma model seems to provide a good framework for describing and understanding the LIBS data of this study.

Since the fitted spectra are simulated without any temporal evolution, the method relies on temporally resolved measurements and is therefore not directly applicable to any LIBS spectrum measured on the Martian surface by the ChemCam instrument [1] that are temporally and spatially integrated. Adapting the plasma model for the description of time integrated measurements would require a much higher model complexity. Furthermore, the computation time of a spectrum already takes several hours on a standard computer and adding extra model parameters for describing any temporal evolution would make the computation time even longer. However, the fact that a two-zone model is able to describe the vast majority of the observed emission lines from different elements with different ionization energies and electronic levels, indicates that simulated spectra from a LTE model could be incorporated directly for at least line identification purposes. One approach would be to simulate spectra from pure elements using the two-zone model with several model parameters extrapolated by the fitted values of this study. A superposition of the spectra could then be projected onto spatially and temporally integrated data with the two zones describing the spatial variations and the superposition for approximating the temporal dimension.

Declaration of Competing Interest

The authors declare that they have no known competing financial interests or personal relationships that could have appeared to influence the work reported in this paper.

Acknowledgments

The author P. B. Hansen thanks and acknowledges the Deutsches Zentrum für Luft- und Raumfahrt (DLR) and the German Academic Exchange Service (DAAD) for financial support via the DLR-DAAD research fellowship program.

References

[1] R.C. Wiens, S. Maurice, J. Lasue, O. Forni, R.B. Anderson, S. Clegg, S. Bender, D. Blaney, B.L. Barraclough, A. Cousin, L. Deflores, D. Delapp, M.D. Dyar, C. Fabre, O. Gasnault, N. Lanza, J. Mazoyer, N. Melikechi, P.Y. Meslin, H. Newsom, A. Ollila, R. Perez, R.L. Tokar, D. Vaniman, Pre-flight calibration and initial data processing for the ChemCam laser-induced breakdown spectroscopy instrument on the Mars Science Laboratory rover, Spectrochim. Acta - Part B At. Spectrosc. 82 (2013) 1–27.

[2] W. Ren Xin, Cai Tingni, Liu Dawei, Liu Jianjun, Zhang Hongbo, Fu Qiang, Xu Zhang Zhoubin, Preliminary Scientific Exploration Programs for Mars Surface Composition Detection Package of China's First Mars Exploration, European Planetary Science Congress, Berlin, Germany, 2018.

[3] R.C. Wiens, S. Maurice, F.R. Perez, The SuperCam remote sensing instrument suite for the Mars 2020 rover mission: a preview, Spectroscopy 32 (5) (2017) 50–55.

[4] K. Knight, L. Scherbarth, A. Cremers, J. Ferris, Characterization of laser-induced breakdown spectroscopy (LIBS) for application to space exploration, Appl. Spectrosc. 54 (3) (2000) 331–340.

[5] G. Cristoforetti, A. De Giacomo, M. Dell'Aglio, S. Legnaioli, E. Tognoni, V. Palleschi, N. Omenetto, Local thermodynamic equilibrium in laser-induced breakdown spectroscopy: beyond the McWhirter criterion, Spectrochim. Acta - Part B At. Spectrosc. 65 (1) (2010) 86–95.

[6] Y. Zhang, Z. Zhao, T. Xu, G. Niu, Y. Liu, Y. Duan, Characterization of local thermodynamic equilibrium in a laser-induced aluminum alloy plasma, Appl. Opt. 55 (10) (2016) 2741.

[7] J. Hermann, C. Boulmer-Leborgne, B. Dubreuil, I.N. Mihailescu, Influence of irradiation conditions on plasma evolution in laser-surface interaction, J. Appl. Phys. 74 (5) (1993) 3071–3079.

[8] A. Bogaerts, Z. Chen, R. Gijbels, A. Vertes, Laser ablation for analytical sampling: what can we learn from modeling? Spectrochim. Acta - Part B At. Spectrosc. 58 (12) (2003) 1867–1893.

[9] S.V. Shabanov, I.B. Gornushkin, Two-dimensional axisymmetric models of laser induced plasmas relevant to laser induced breakdown spectroscopy, Spectrochim. Acta - Part B At. Spectrosc. 100 (2014) 147–172.

[10] J. Hermann, A. Lorusso, A. Perrone, F. Strafella, C. Dutouquet, B. Torralba, Simulation of emission spectra from nonuniform reactive laser-induced plasmas, Phys. Rev. E Stat. Nonlinear Soft Matter Phys. 92 (2015) 5.

[11] J.A. Aguilera, C. Aragón, J. Bengoechea, Spatial characterization of laser-induced plasmas by deconvolution of spatially resolved spectra, Appl. Opt. 42 (30) (2003) 5938–5943.

[12] A. Kramida, Y. Ralchenko, J. Reader, NIST Atomic Spectra Database Team, NIST Atomic Spectra Database (version 5.3), 2015.

[13] STARK-B, Database for "Stark" Broadening of Isolated Lines of Atoms and Ions in the Impact Approximation, 2021.

[14] M. Burger, J. Hermann, Stark broadening measurements in plasmas produced by laser ablation of hydrogen containing compounds, Spectrochim. Acta - Part B At. Spectrosc. 122 (2016) 118–126.

[15] S. Zielinska, S. Pellerin, K. Dzierzega, F. Valensi, K. Musiol, F. Briand, Measurement of atomic Stark parameters of many MnI and Fe I spectral lines using GMAW process, J. Phys. D. Appl. Phys. 43 (2010).

[16] S. Kirkpatrick, C.D. Gelatt, M.P. Vecchi, Optimization by simulated annealing, Science 220 (4598) (1983) 671–680.

[17] A. De Giacomo, Experimental characterization of metallic titanium-laser induced plasma by time and space resolved optical emission spectroscopy, Spectrochim. Acta - Part B At. Spectrosc. 58 (11) (2003) 71–83.

[18] L. Mercadier, J. Hermann, C. Grisolia, A. Semerok, Plume segregation observed in hydrogen and deuterium containing plasmas produced by laser ablation of carbon fiber tiles from a fusion reactor, Spectrochim. Acta - Part B At. Spectrosc. 65 (8) (2010) 715–720.

[19] J. Hermann, D. Grojo, E. Axente, C. Gerhard, M. Burger, and V. Craciun, "Ideal radiation source for plasma spectroscopy generated by laser ablation," Phys. Rev. E, vol. 96, p. 53210, nov 2017.